ACS APPLIED NANO MATERIALS

www.acsanm.org Article

Tuning Crystal Morphology in MOFs for Improved Hydrogen Storage

Ruthradharshini Murugavel, Ali A. Rownaghi, and Fateme Rezaei*

Cite This: *ACS Appl. Nano Mater.* 2024, 7, 23733−23743 Read Online

ACCESS | Metrics & More | Article Recommendations | Supporting Information

ABSTRACT: Achieving net-zero carbon emissions by 2050 is imperative to mitigating the global climate crisis, necessitating a transition to sustainable energy sources. Hydrogen, recognized for its high energy density, is a promising sustainable fuel; however, its storage and transportation are challenging, necessitating the development of more effective storage materials. Metal−organic frameworks (MOFs) possess exceptional structural integrity and diversity, making them highly valuable in applications such as catalysis, separations, and energy storage. Despite their significant potential as viable materials for H_2 storage, the poor packing of powdered MOFs limits their volumetric storage capacity. Improvement in packing density can be achieved by modifying the crystal shape and structure to reduce the void volume. In this paper, we embarked on synthesizing different nonideal crystal shapes and orientations by varying the ligand-to-metal ratio, which changes the overall crystal growth direction. We report the engineering of MIL-53-Al, focusing on tuning its crystal size and shape distribution to enhance its packing density and volumetric H_2 storage capacity. This approach allows the synthesis of MOF nanomaterials with a high surface area (up to 1900 m^2/g) and increased packing density (0.38 g/cm^3), while preventing crystal damage when subjected to pressure compaction, thereby enhancing the volumetric storage capacity. After tuning, the volumetric storage capacity of the two best-performing samples, $(MIL\text{-}53\text{-}Al)_{1:1}$ and $(MIL\text{-}53\text{-}Al)_{0.52:1}$, exhibited a monoclinic crystal shape, which enhanced not only the overall packing density but also the working volumetric capacity of the system. Specifically, $(MIL\text{-}53\text{-}Al)_{1:1}$ achieved an enhancement of 25% in working capacities compared to pristine MIL-53-Al. Moreover, its volumetric working capacity was estimated to be 37 g/L under the pressure swing (PS) conditions between 77 K/70 bar and 77 K/5 bar, surpassing the 30 g/L volumetric capacity of the compressed 700-bar pressure storage systems.

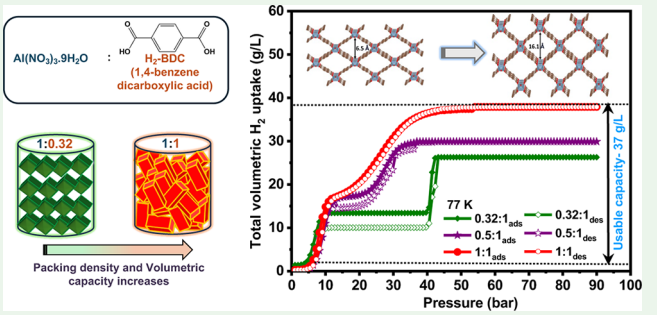

KEYWORDS: *H_2 storage, metal−organic frameworks, crystal morphology, working capacity, breathing transition, MIL-53-Al*

1. INTRODUCTION

Natural gas and hydrogen (H_2) are increasingly recognized as pivotal in the transition toward a more sustainable and low-carbon energy future. As global concerns about climate change and environmental sustainability grow, both fuels offer promising pathways to reduce greenhouse gas emissions while meeting the world's ever-increasing energy demands. Natural gas, primarily composed of methane, is considered a cleaner alternative to traditional fossil fuels, with lower carbon emissions, making it a key transitional energy source.[1,2] H_2, on the other hand, is seen as a long-term solution, particularly because of its potential to serve as a zero-emission fuel when produced from renewable sources or when coupled with carbon capture technologies.[3,4]

The quest for an optimal sorbent material for H_2 storage remains a significant challenge in the transition to the H_2 economy has a low energy density by volume, making its storage both a technical and economic hurdle. Various technologies have been explored to enhance the energy density of H_2 storage, including physical methods[5] (e.g., cold, cryo, or cryo-compressed systems) and material-based approaches[6] (e.g., physisorbents, chemical H_2 storage materials, and metal hydrides). Physisorbents, including activated carbons,[7−10] metal−organic frameworks (MOFs),[11−13] covalent organic frameworks (COFs),[14−17] porous organic polymers (POPs),[18,19] and zeolites,[20−22] have gained attention due to their high storage capacity at cryogenic temperatures, reversibility, and fast kinetics. In this context, our recent study[23] demonstrated how optimizing the ultramicropore volume to 1.23 cm^3/g in resorcinol-formaldehyde (RF)-derived aerogels, with an exceptionally high surface area of

Received: July 18, 2024
Revised: September 18, 2024
Accepted: September 19, 2024
Published: October 15, 2024

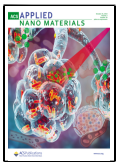

https://doi.org/10.1021/acsanm.4c04072
ACS Appl. Nano Mater. 2024, 7, 23733−23743

3200 m^2/g, creates ideal conditions for H_2 adsorption. This resulted in gravimetric and volumetric storage capacities of up to 2.1 wt % and 6.8 g/L at 298 K and 100 bar. Under cryogenic conditions, the aerogels exceeded the DOE gravimetric target, achieving up to 6.8 wt % and 28 g/L at 77 K and 100 bar.

Among the physisorbent materials, H_2 storage in MOFs[24] stands out as one of the most promising approaches due to their rapid kinetics, reversibility, tunable pore structure, and high gravimetric capacities.[12,13,25,26] However, a primary challenge with MOFs is their low affinity toward H_2 at ambient temperature, stemming from the weak interaction between H_2 molecules and the MOF surface. To address this, several strategies have been proposed. One approach is to incorporate high-affinity sites into MOFs, which can enhance the H_2-binding interaction.[27] Another strategy involves optimizing the pore size and structure of MOFs to better accommodate H_2 molecules, thus improving the adsorption performance. For example, Zhang et al.[28] synthesized the H_2-bonded organic framework RP-H101 using a controlled catenation strategy to achieve a favorable balance between gravimetric and volumetric surface areas (3526 m^2/g vs 1885 m^2/cm^3). The framework also exhibited a total pore volume of 1.35 cm^3/g and an optimal pore diameter of 1.7 nm, resulting in an enhanced H_2 uptake capacity of 1.5 wt % and 9.6 g/L. Additionally, H_2-spillover materials, such as metal nanoparticles[29,30] and heteroatoms[29] can facilitate H_2 uptake by transferring hydrogen atoms from the metal to the MOF surface. Modifying the MOF framework to create more favorable conditions for H_2 adsorption, such as adjusting framework flexibility or using mixed-metal MOFs, further enhances performance.[27,31] Furthermore, operating MOFs under optimized temperature and pressure conditions can also improve their H_2 storage performance, while combining MOFs with other materials (e.g., carbon-based supports or polymers) can create hybrid systems with enhanced properties.[32] Despite these advancements, achieving high volumetric capacities in MOFs remains challenging due to their highly porous structure, the nature of their binding energy toward H_2, and the relatively low packing density of powdered MOFs, which limit their practical applicability in on-board storage systems.

To address this limitation, various densification strategies such as pelletization, monolith formation with or without binders,[33−35] and direct ink writing (DIW)[36] printing have been explored. These approaches aim to improve the packing density of MOFs, thereby reducing void spaces within the structure and enhancing the overall storage capacity. For instance, Hirscher et al.[37] demonstrated that pelletization synthesized through a mechanochemical approach could improve the volumetric capacity of MOFs without significantly compromising their surface area and adsorption properties. Similarly, Tian et al.[38] utilized monolith formation without binders and demonstrated achieving higher packing densities in MOFs, resulting in enhanced storage capacities. Nevertheless, achieving optimal packing density in the range of 0.4−0.5 g/cm^3 while preserving the structural integrity and accessible binding sites of MOFs is a complex challenge.[39] The intrinsic porosity and structural diversity of MOFs, which facilitate gas adsorption, also present difficulties in attaining high volumetric storage capacities.

The Hydrogen Storage Engineering Center of Excellence (HSECoE) has demonstrated that inefficient material packing can lead to a reduction of 60% in volumetric capacity compared to single crystal packing.[40] Modifying the crystal morphology of the MOFs can potentially overcome this challenge. By carefully adjusting the ligand-to-metal ratio during synthesis, the growth direction and morphology of the MOF crystals can be controlled, leading to improved packing efficiency and reduced void volume. This approach has been supported by various studies, such as those by Suresh et al.,[41] who demonstrated that engineering the crystal size and shape of MOFs could significantly enhance their packing density to 0.38 g/cm^3 (up to 100% improvement) and the volumetric storage capacity of 30.5 g/L for MOF-5.

Motivated by the studies of optimizing the MOF structure to enhance packing density, this research focuses on engineering MOFs with tailored crystal shapes to improve working volumetric H_2 storage capacity driven by their adsorption-based structural transitions. These transitions can also be influenced by changes in particle size, crystal habit, pore structure, and connectivity. Specifically, the study targets the synthesis and tuning of MIL-53-Al, an MOF noted for its high surface area, breathing effect potential in H_2 storage, and relatively low synthesis cost. The novelty of this work lies in the engineering of MOFs through the modification of crystal morphology, enhancing packing density, and inducing step-shaped isotherm resulting from H_2 adsorption driving the structural phase transition upon the MOFs' external stimuli of temperature and pressure. Through controlled synthesis methods, we manipulated the crystal size and shape distributions of MIL-53-Al. The resultant MOF samples, exhibiting a bimodal crystal shape distribution of monoclinic and orthorhombic crystal structures, demonstrated significant enhancements in both packing density and volumetric working capacity. These findings indicate that strategic tuning of MOF crystals' morphology can effectively mitigate the limitations of low packing density, rendering MOFs a more practical and efficient option for H_2 storage. The optimized samples not only surpassed the volumetric capacity of compressed storage systems but also showed potential in meeting the Department of Energy's 2025 targets for storage, if a storage system is designed to meet the targets by 20%.

2. EXPERIMENTAL SECTION

2.1. Materials. The following materials were used for sorbent synthesis without further purification: aluminum(III) nitrate nonahydrate ($Al(NO_3)_3{\cdot}9H_2O$, 99.55%) and 1,4-benzenedicarboxylic acid (H_2−BDC, 98%) were used as the Al (metal precursor) and organic ligand, respectively. In addition, *N*,*N*′-dimethylformamide (DMF, 99.8%), hydrochloric acid (HCl, 37% N), methanol (CH_3OH, 99.8%), and deionized (DI) water was used in this study. All materials were purchased from Sigma-Aldrich. The ultrahigh purity (UHP) gases, such as H_2, He, and N_2, used in this study were obtained from Airgas.

2.2. Synthesis of MIL-53-Al Sorbents. The synthesis of MIL-53-Al described here followed a modified procedure based on the previously reported ultrasonication-assisted hydrothermal method.[42] Briefly, solutions of $Al(NO_3)_3{\cdot}9H_2O$ and H_2−BDC in DI water were mixed and sonicated for 30 min at room temperature (20 ± 1 °C) and then loaded into an oven at 220 °C for 24 h. The mass ratio of the organic ligand to metal salt precursor (L:M) varied from 0.22:1 to 1:1. After the autoclave cooled down, the solid phase was separated using a centrifuge, and 35 mL of DMF solution was added to remove unreacted terephthalic acid trapped in the pores of the samples. The autoclave was placed back in the oven and heated to 150 °C for 12 h. After centrifugation, the solid was kept in a Falcon tube and washed three times with methanol. The obtained powder sample was then immersed in methanol and dried in the oven at 150 °C under vacuum

https://doi.org/10.1021/acsanm.4c04072
ACS Appl. Nano Mater. 2024, 7, 23733−23743

overnight. Figure 1 shows the proposed synthetic mechanism in this work.

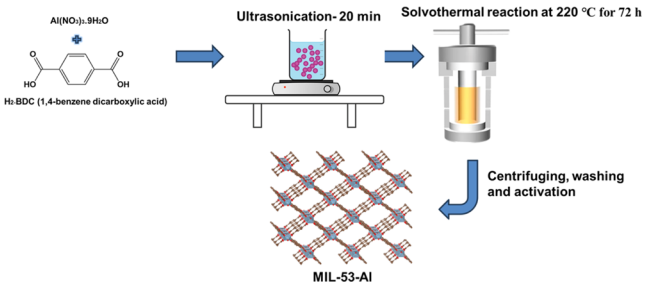

Figure 1. Schematic representation of ultrasonicated-assisted MIL-53-Al synthesis.

2.3. Materials Characterization. The MOF sample's textural properties were evaluated through N_2 physisorption experiments conducted at 77 K within a pressure range of 0 to 1 bar on a Micromeritics (3Flex) gas analyzer. Prior to analysis, samples were degassed under vacuum for 12 h at their respective degassing temperatures on a Micromeritics Smart VacPrep instrument. The surface area, pore volume, and pore size distribution (PSD) were determined using the Brunauer–Emmett–Teller (BET), Dubinin–Radushkevich (DR), Barrett–Joyner–Halenda (BJH), and density functional theory (DFT) methods, respectively at P/P_0 = 0.9. Total pore volumes were calculated by integrating the PSDs for pores sized: (i) under 2 nm (V_{micro}), i.e., micropores, and (ii) between 2 and 50 nm (V_{meso}), i.e., mesopores, as calculated by V_T–V_{micro}. Total (d_p) average pore sizes were calculated based on volume-weighted average. The skeletal density was determined using a helium (He) pycnometer in a Micromeritics AccuPyc II 1340 instrument at room temperature. The packing density of the samples was assessed through tapped density analysis using an AS-100 tap density volumeter. The crystallinity of the samples was analyzed by X-ray diffraction (XRD) on a PANalytical X'pert multipurpose X-ray diffractometer with a scan step size of 0.02°/step and a rate of 147.6 s/step. The structure and surface topography of the MOF were examined using a Hitachi S4700 field-emission scanning electron microscope (FE-SEM). Energy dispersive X-ray spectroscopy (EDS) data were collected alongside SEM images and analyzed using Genesis software to determine the elemental analysis across the MOF samples. X-ray photoelectron spectroscopy (XPS) was obtained using a Kratos Axis 165 photoelectron spectrometer with an aluminum X-ray source to excite the samples. Fourier-transform infrared (FTIR) spectroscopy was conducted with a Nicolet FTIR iS50 Model instrument to determine structural or chemical differences between the samples.

3. RESULTS AND DISCUSSION

3.1. General Textural Characterization of Sorbents. The N_2 physisorption isotherms and PSD profiles of the MOFs obtained at 77 K are illustrated in Figure 2, while the corresponding textural properties are outlined in Table 1. All

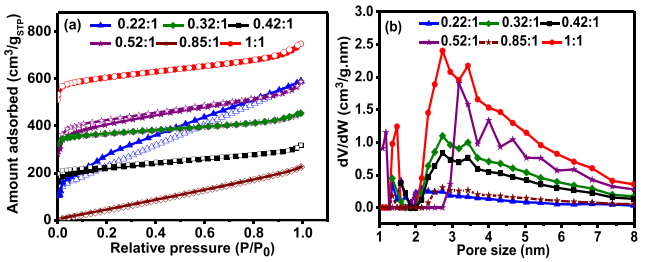

Figure 2. (a,c) N_2 physisorption isotherms and (b) PSD profiles of MIL-53-Al sorbents.

sorbents exhibited type Ia isotherms, indicating their hierarchical microporous–mesoporous structure, as per the IUPAC classification of isotherms.[43] The PSD profiles in Figure 2b confirmed the existence of both micropore and mesopore volume ranges of pore sizes 2–10 nm, while Figure S1 highlights the micropore distribution for these sorbents. The control sample, $(MIL\text{-}53\text{-}Al)_{0.22:1}$, demonstrated a type I isotherm with an H4 hysteresis loop, having the S_{BET} (BET surface area) of around 1130 m^2/g, total V_p (pore volume) of around 0.65 cm^3/g, and an average pore size diameter of 0.95 nm. This S_{BET} value is comparable to the reported value (1204 m^2/g) in the literature.[42,44] A lower ligand ratio of 0.22 showed a higher mesopore volume of 0.4 cm^3/g, likely due to less efficient packing and more voids within the structure. Increasing the L:M ratio had notable effects on the S_{BET} and V_p, as summarized in Table 1. Among the MOF sorbents synthesized with varying L:M ratios, $(MIL\text{-}53\text{-}Al)_{1:1}$ exhibits a type Ia isotherm and displayed one of the highest S_{BET} values (ca. 1906 m^2/g), total V_p (ca. 0.94 cm^3/g), and an average pore diameter in the range of 1.34 nm, surpassing previously reported values.[45] The specific surface area and average pore size are greater than those of the conventionally synthesized MIL-53-Al in the literature. The higher L:M ratio enhanced the microporosity of about 0.55 cm^3/g and packing density of 0.38 g/cm^3, suggesting a more densely packed and efficient crystal structure. This trend was consistent with the $(MIL\text{-}53\text{-}Al)_{0.52:1}$ sample, which exhibited a S_{BET} of ~1438 m^2/g and a pore volume of 0.85 cm^3/g, showing a shift toward ultramicropores (<2 nm). This suggested a more complete coordination environment, promoting the formation of a denser microporous framework. Overall, increasing the L:M ratio optimized the formation of a well-coordinated, extended framework with minimal defects, maximizing the internal specific surface area and porosity. The abundance in organic linker concentration promotes complete coordination and connectivity within the framework.[46,47] However, while the specific surface area was on an increasing trend, one of the samples, $(MIL\text{-}53\text{-}Al)_{0.85:1}$, displayed the lowest surface area of 832 m^2/g and V_p of ~0.5 cm^3/g, which can be attributed to incomplete coordination and dissolution of the crystal structure. This was evidenced from the TGA profiles in Figure S2a, which showed 15.85% weight loss occurring between 150 and 400 °C, originating from. This weight loss originated the degradation of the framework due to weaker coordination bonds between Al–O and Al–ligand, and resulting in a less stable structure.[47] Additionally, the early onset of decomposition below 450 °C, along with a broader and more gradual weight loss, further indicated a less stable framework and incomplete coordination. This degradation was also reflected in the XRD pattern (Figure S2b) of $(MIL\text{-}53\text{-}Al)_{0.85:1}$, where the intensity was significantly lower than that of the simulated pattern, suggesting an incomplete framework structure.

The total pore volume, on the other hand, exhibited a more substantial variance, with $(MIL\text{-}53\text{-}Al)_{1:1}$ having a V_p of 0.94 cm^3/g, whereas $(MIL\text{-}53\text{-}Al)_{0.22:1}$ showed 0.65 cm^3/g, indicating a 30% decrease in the total pore volume, which stemmed from the increase in the micropore volume. This increase in microporosity resulted from enhanced coordination and connectivity within the framework, leading to denser packing and reduced interparticle voids. The correlation between BET analysis and PSD profiles (Figure S3) further reinforced this, with samples such as $(MIL\text{-}53\text{-}Al)_{1:1}$ displaying high surface areas (ca. 1906 m^2/g) and dominant peaks in the

https://doi.org/10.1021/acsanm.4c04072
ACS Appl. Nano Mater. 2024, 7, 23733–23743

Table 1. Textural Properties of MIL-53-Al Sorbents

Sorbent (L:M)	$S_{BET}[S_{\mu p}]$ (m^2/g)[a]	V_{tot} (cm^3/g)[b]	$V_{1.7-25\ nm}$ (cm^3/g)[c]	$V_{>25\ nm}$ (cm^3/g)[d]	$V_{\mu p\ (<1.7\ nm)}$ (cm^3/g)[e]	$d_{p\ via\ NLDFT}$ (nm)[f]	$\rho_{packing}$ (g/cm^3)[g]
0.22:1	1130[935]	0.65	0.4	0.02	0.23	0.95	0.23
0.32:1	1253[1010]	0.73	0.23	0.08	0.42	1.08	0.28
0.42:1	1165[824]	0.7	0.22	0.10	0.38	1.13	0.32
0.52:1	1438[1035]	0.85	0.27	0.10	0.48	0.87	0.35
0.85:1	832[476]	0.5	0.23	0.13	0.14	1.21	0.31
1:1	1906[1185]	0.94	0.30	0.09	0.55	1.34	0.38

[a]The first number indicates the BET surface area; the number in the square brackets indicates the micropore area given by the *t*-plot. [b]The single highest volume of N_2 adsorbed in the adsorption isotherm at 77 K (where $P/P_0 \sim 0.997$). [c]Mesopore volume obtained from Barrett, Joyner, and Halenda (BJH). [d]Via $V_{>25\ nm} = V_{tot} - (V_{1.7-25} + V_{\mu p<1.7\ nm})$. [e]The micropore volume ($V_{\mu p}$) was calculated via the Dubinin–Radushkevich (DR) and density functional theory (DFT) methods on N_2 adsorption up to 1 bar at 77 K. [f]Calculated as indicated using the NLDFT method. [g]Calculated from the tapped density analysis.

microsize range (0.08 μm), indicative of extensive microporosity. Conversely, samples with broader particle size distributions, such as $(MIL\text{-}53\text{-}Al)_{0.85:1}$, exhibited lower surface areas and an increased presence of larger mesopores. The PSD profiles, as assessed through the Microtrac S3500 diffraction analyzer, showed a clear trend where smaller and more uniform particles corresponded to higher surface area and greater microporosity, as noted in the $(MIL\text{-}53\text{-}Al)_{0.32:1}$, $(MIL\text{-}53\text{-}Al)_{0.52:1}$, and $(MIL\text{-}53\text{-}Al)_{1:1}$ samples. This trend was further confirmed by the gradual broadening of particle size distributions in samples with lower surface areas, particularly those with more meso- and macro-sized particles. Overall, the BET and particle size data aligned to demonstrate how enhanced coordination within the framework improved the structural integrity and uniformity of the samples.

Consequently, the overall packing density increased, as evidenced by the measured packing density of $(MIL\text{-}53\text{-}Al)_{1:1}$ at 0.38 g/cm^3, in closer agreement with the crystallographic (0.978 g/cm^3)[48] and powder density (0.23 g/cm^3)[45] of conventional $(MIL\text{-}53\text{-}Al)_{0.22:1}$. The optimized packing density analysis of the samples is detailed in Section S4. This analysis indicated a more efficient packing arrangement, suggesting tighter packing between crystals and contributing to improved structural integrity and reduced interparticle voids.

3.2. Structure and Morphology of Sorbents. To investigate the structural and morphological characteristics of the synthesized MIL-53-Al sorbents, XRD analysis was performed, and the corresponding diffraction patterns are shown in Figure 3. The experimental spectra of the sorbents were consistent with the simulated pattern, indicating that the structural integrity was preserved upon varying L:M ratios. The characteristic XRD pattern of the simulated MIL-53 topology exhibited a series of intense and well-resolved peaks at 2θ values of around 9.0°, 10.2°, 12.2°, 16.6°, and 17.4°, which were assigned to the (101), (200), (110), (011), and (202) indices, respectively, of the MIL-53 framework.[47] Specifically, the peaks at 2θ = 9.0° corresponded to the growth along the (101) plane in the orthorhombic (np) crystal structure of MIL-53-Al.[47] This np pattern was prominent in samples with L:M ratios of 0.22:1, 0.32:1, and 0.42:1, implying the preservation of the orthorhombic phase in these ratios. The decrease in the intensity of the peak at 2θ = 9.0° observed in samples with higher L:M ratios was a key indication of the structural transformation, leading to changes in the crystal shape and volume.[49] The shift and emergence of new peaks around 12.5° are typically associated with the growth along the (110) plane corresponding to the monoclinic phase structure.[47] This phase transition was characterized by the rearrangement of the framework influenced by the increased concentration of the ligand, promoting coordination and connectivity within the structure. This pattern agrees with the monoclinic large pore (lp) simulated structure obtained from the literature.[50]

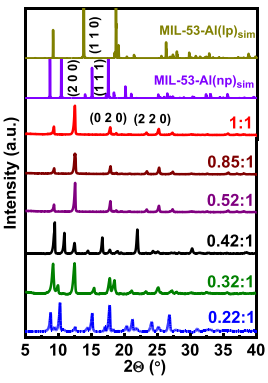

Figure 3. XRD patterns of MIL-53-Al sorbents.

It is worth noting that the MIL-53 framework is known to exhibit structural flexibility, where the pore dimensions can change depending on the guest molecules present or the activation conditions. This flexibility can lead to variations in the relative intensities of the XRD peaks, as observed in the different patterns shown in Figure 3, possibly due to the varying L:M ratios, increasing the nucleation rate of crystal formation during synthesis.

All of the structures were refined with Fullprof using the WinPLOTR software package. The atomic coordinates for the synthesized forms of MIL-53-Al are given in Table 2. The transition from the orthorhombic to the monoclinic phase is also reflected in the lattice parameters and cell volumes of the MOFs. For instance, the orthorhombic crystal system samples (0.22:1, 0.32:1, and 0.42:1) showed lattice parameters of $a \approx$ 16.2–16.6 Å, $b \approx$ 6.2–6.6 Å, and $c \approx$ 5.5–5.6 Å, with cell volumes of ~560–608 $Å^3$. In contrast, the monoclinic samples (0.52:1, 0.85:1, and 1:1) exhibited larger cell volumes of 1359–1422 $Å^3$, with lattice parameters of $a \approx$ 6.2–6.9 Å, $b \approx$ 16.4–17.2 Å, and $c \approx$ 12.6–12.9 Å. The increase in the L:M ratio enhanced the nucleation rate of crystal formation, promoting a structural transformation that increased the packing density. This shift from the orthorhombic to the monoclinic phase resulted in a more densely packed structure,

https://doi.org/10.1021/acsanm.4c04072
ACS Appl. Nano Mater. 2024, 7, 23733–23743

Table 2. Unit Cell Parameters and Volume of MIL-53-Al Sorbents

Sorbent (L:M)	Crystal system	Space group	Lattice parameters (Å)			Cell volume (Å)^3
			a	*b*	*c*	
0.22:1	orthorhombic	*Pnma*	16.64	6.64	5.50	607.69
0.32:1	orthorhombic	*lmma*	16.21	6.20	5.57	559.74
0.42:1	orthorhombic	*lmma*	16.24	6.21	5.59	563.75
0.52:1	monoclinic	*Cc*	6.89	16.41	12.58	1422.35
0.85:1	monoclinic	*Cc*	6.71	16.42	12.61	1359.34
1:1	monoclinic	*Cc*	6.20	17.20	12.95	1380.89

as indicated by the larger cell volumes and the appearance of new diffraction peaks, as discussed earlier.

The SEM micrographs of the as-synthesized MIL-53-Al samples are shown in Figure 4. As observed in Figure 4a,

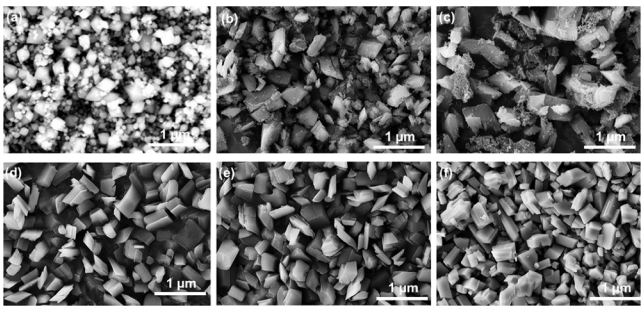

Figure 4. SEM images of MIL-53-Al sorbents with L:M ratios of (a) 0.22:1, (b) 0.32:1,(c) 0.42:1, (d) 0.52:1, (e) 0.85:1, and (f) 1:1.

$(MIL\text{-}53\text{-}Al)_{0.22:1}$ exhibited a regular octahedral-shaped prism morphology with an average uniform crystal size of 81 nm. In contrast, $(MIL\text{-}53\text{-}Al)_{0.32:1}$ and $(MIL\text{-}53\text{-}Al)_{0.42:1}$ in Figure 4b,c displayed orthorhombic-shaped crystals with an average size of 150 nm. The $(MIL\text{-}53\text{-}Al)_{0.22:1}$ sample with the lowest L:M ratio gave rise to smaller-sized crystals compared to those with higher ratios, mainly due to the faster nucleation relative to the crystal growth rate.[51] With further increase in ligand concentration, the $(MIL\text{-}53\text{-}Al)_{0.52:1}$ and $(MIL\text{-}53\text{-}Al)_{1:1}$ samples in Figure 4d–f showed a balance between growth and nucleation rates, thereby leading to the formation of a more uniform monoclinic crystal system. At higher L:M ratios, an excess of ligand lead to a more controlled nucleation process. This resulted in a larger number of smaller nucleation sites, leading to the formation of smaller crystals. This agreed well with the particle size distribution data, as discussed in Section S3. This phenomenon of crystal shape and size transition with increased ligand concentration played a crucial role in determining the crystal size and morphology of the sorbents. Such notable change correlated with the enhanced BET surface area, peaking at 1900 m^2/g. Notably, the transition from orthorhombic to monoclinic phases enhanced the surface area and packing density by improving crystal habit and reducing interstitial voids, thereby increasing pore volume, as noted in Table 1.

The EDS energy spectrum analysis of the SEM images was performed to image the elemental composition and distribution on the synthesized sorbents, as shown in Figure 5. Figure 5b–d reveals the distribution of C, O, and Al elements consistent with the expected composition of MIL-53-Al. The uniform distribution of Al throughout the frameworks indicated a well-connected crystalline MOF structure. This suggested that increasing the ligand concentration up to a 1:1

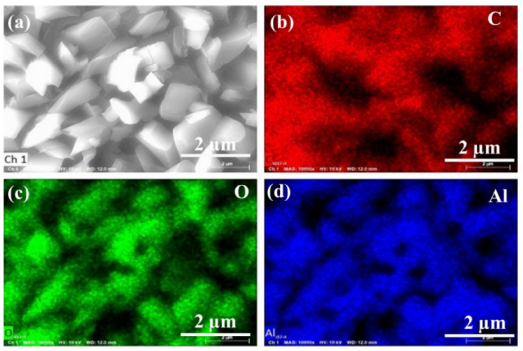

Figure 5. SEM micrograph of (a) $(MIL\text{-}53\text{-}Al)_{1:1}$ and (b–d) the corresponding EDS elemental distribution of C, O, and Al, respectively.

ratio promotes the formation of a robust crystalline structure, ensuring well-integrated metal nodes and preventing any dissolution within the framework.

The EDS spectral analysis also reveals the surface chemistry and chemical states of C, O, and Al elements in the as-synthesized MIL-53-Al samples, as shown in Figure 6a. The peaks in the C 1s spectrum seen in Figure 6b, at 289.4 and 284.8 eV, corresponded to the O—C═O and C–C bonds, respectively, present in the secondary building units of the MIL-53-Al structure. In Figure 6c, the O 1s spectra at 531.9 eV were assigned to the oxygen species in the carboxylate linker, including the O—C═O, C–OH, O–Al, and C–C bonds. Additionally, the characteristic peaks at a binding energy of 74.87 eV represented Al 2p, as shown in Figure 6d. As the ligand concentration increased, there was a noticeable increase in the intensities of the C 1s and O 1s peaks, which made sense since the organic linkers contain carbon and oxygen atoms; hence, their increased concentration results in more pronounced C and O peaks in the EDS spectra.

Moreover, the highest L:M ratio sample of 1:1 exhibited a significant increase in the intensity of the Al 2p peaks. This phenomenon was due to the enhanced crystallinity and a better-coordinated MOF structure at higher ligand concentrations. The well-defined monoclinic crystal structure at this ratio exposes more aluminum nodes, which are essential for the formation of the MIL-53-Al framework. Such increase in the Al 2p peak intensity correlated well with the structural transition observed, where the crystals shifted from smaller orthorhombic shapes at lower ligand concentrations to larger monoclinic shapes at higher ligand concentrations. This transition was driven by the interplay between nucleation and crystal growth rates, with higher ligand concentrations favoring crystal growth over nucleation, resulting in the formation of larger monoclinic crystals. At lower ligand concentrations, nucleation occurs rapidly, leading to smaller crystal sizes, but as the ligand concentration increases, the crystal growth rate becomes more

https://doi.org/10.1021/acsanm.4c04072
ACS Appl. Nano Mater. 2024, 7, 23733–23743

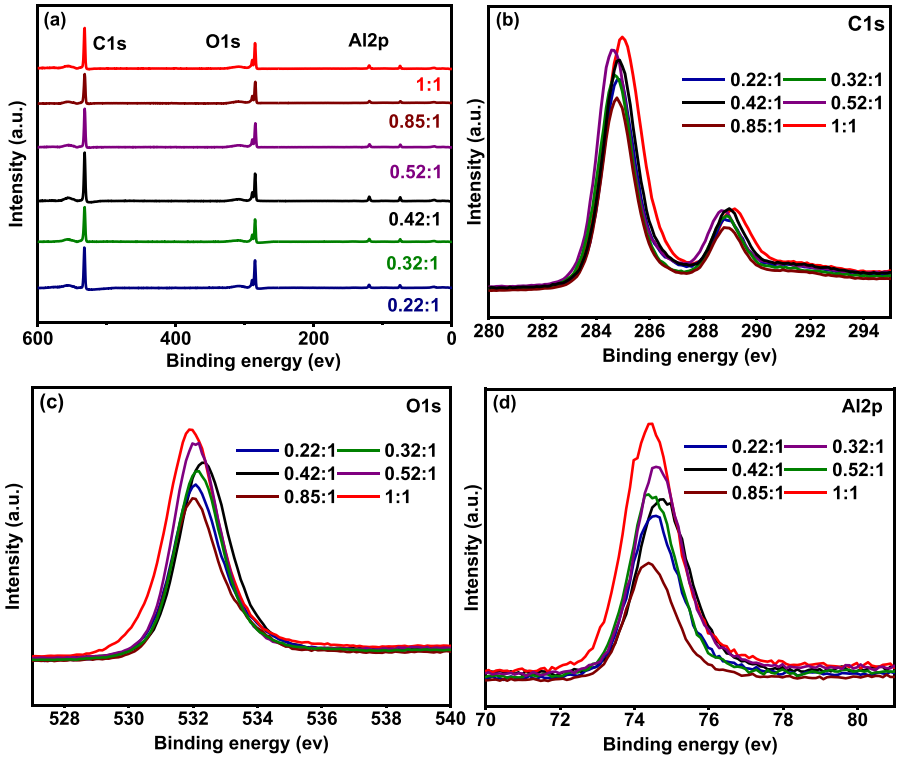

Figure 6. (a) Overall XPS survey spectra and high-resolution spectra of (b) C 1s, (c) O 1s, and (d) Al 2p states of MIL-53-Al sorbents.

comparable to the nucleation rate, resulting in larger, more uniform crystals. This transition enhanced the exposure of both metal nodes (Al) and organic linkers (C, O), leading to the observed increase in peak intensities in the EDS spectra. Overall, the EDS results confirmed the unaltered chemical states of the respective elements in the as-synthesized MIL-53-Al samples. The EDS elemental compositions are listed in Table S2.

3.3. High-Pressure H_2 Adsorption Isotherms. The high-pressure adsorption isotherms at 298 K for MIL-53-Al samples with varying L:M ratios revealed significant insights into structure-performance relations, as shown in Figure 7. The

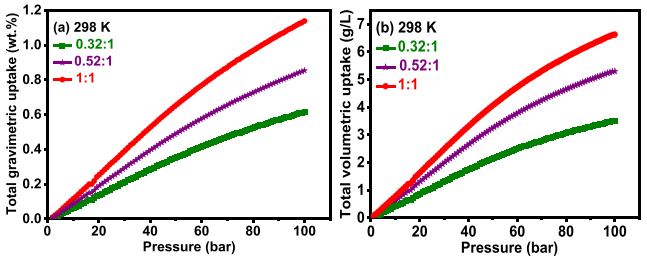

Figure 7. High-pressure total (a) gravimetric and (b) volumetric H_2 adsorption isotherms for MIL-53-Al sorbents at 298 K.

total gravimetric and volumetric capacities were calculated using eqs S1−S3 as given in Section S5. As noted inFigure 7a, the H_2 uptake increased upon increasing the L:M ratio. The 1:1 sample exhibited the highest gravimetric uptake, reaching approximately 1.2 wt % at 100 bar, followed by the 0.52:1 sample with an uptake of ∼0.9 wt %, and the 0.32:1 sample with the lowest uptake of approximately 0.6 wt % at the same pressure. Previous studies in the literature have emphasized that the H_2 adsorption capacity of MOFs is directly proportional to their specific surface area and micropore volume. The same trend was observed in the higher ligand concentrations, as it gave rise to higher H_2 adsorption by enhancing the surface area and the total pore volume, specially in the case of $(MIL\text{-}53\text{-}Al)_{1:1}$ sample. The growth direction for the monoclinic phase, typically along the (010) direction, supported the enhanced pore connectivity, resulting in higher H_2 uptake. In contrast, the orthorhombic phase, prevalent in the 0.32:1 sample, with its growth direction along the (111) direction, provided a more rigid and compact structure with limited H_2 adsorption capacity.

Similarly, the volumetric uptake isotherms (Figure 7b) displayed a consistent trend, on account of the increase in the packing density of the sorbents. The 1:1 sample achieved the highest volumetric uptake of ∼5.5 g/L at 100 bar, compared to the 0.52:1 and 0.32:1 samples, which exhibited uptakes of 4.5 g/L and 3.5 g/L, respectively. The volumetric uptake also improved with increasing L:M ratio, suggesting that a higher ligand content enhanced the packing density, as noted in Table 1, and the overall adsorption capacity of the materials. The increase in the packing density of the crystal system up to 0.38 g/cm^3, signified the effect of crystal transition on the reduction of interparticle voids, thereby resulting in increased capacity at higher pressures. Higher ligand content can stabilize the expanded form of the MOF at room temperature, allowing for more gas to be adsorbed. This stabilization reduces the likelihood of framework collapse or reduced pore accessibility, ensuring that the high surface area and pore volume are fully utilized. Notably, the breathing transition characteristic of MIL-53 was not apparent in the room temperature isotherms but became evident at cryogenic temperature. At room temperature, the thermal energy available to the framework maintains it in an expanded state, resulting in a smooth adsorption curve without distinct transitions. At cryogenic

https://doi.org/10.1021/acsanm.4c04072
ACS Appl. Nano Mater. 2024, 7, 23733−23743

temperatures, as discussed in the forthcoming sections, the reduced thermal energy allows for more pronounced structural transitions between the open and closed states of the MOF, manifesting as steps or plateaus in the isotherms. This behavior is consistent with the flexible nature of MIL-53, where the framework can undergo significant structural changes depending on the temperature and adsorption conditions. The error bars in the plot indicated the standard deviation of the data, reflecting the variability and increased sensitivity in the total gravimetric uptake measurements, as detailed in Figure S5.

The cryogenic adsorption isotherms of MIL-53-Al in the pressure range of 0−70 bar are shown in Figure 8. The data

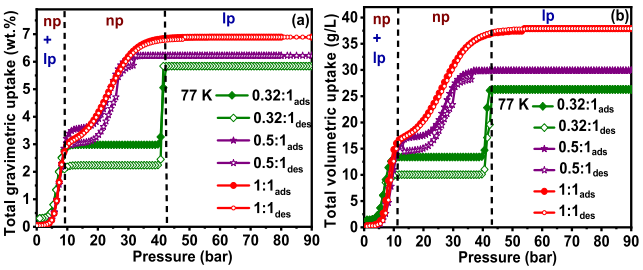

Figure 8. High-pressure (a) gravimetric and (b) volumetric H_2 isotherms at 77 K for MIL-53-Al sorbents.

described the samples with varying L:M ratios to better provide insights onto structure-performance relations in these MOFs. The sample with the L:M ratio of 0.32:1 exhibited a relatively low uptake, plateauing around 5.8 wt % and 26 g/L at high pressure and displaying a distinct two-step adsorption process with hysteresis, indicative of the framework's structural transitions. This behavior is reflective of the breathing effect, characterized by a structural shift from a np to a lp form. According to the literature,[52] the flexible breathing transition in the MIL-53 family—the most extensively studied flexible MOFs—involves molecular adsorption that triggers breathing along one-dimensional channels, leading to changes in pore diameter. The initial dominant np form exhibits constrained adsorption performance, after which increasing pressure triggers a transition to the lp form.[53] This form can accommodate larger volumes but saturates, requiring pressures exceeding 30 bar to achieve maximum H_2 storage capacities. The observed hysteresis indicates that the structural transition involved energy barriers and was not entirely reversible, which may be due to the framework's limited flexibility in this phase.[54] The lower ligand concentration resulted in smaller, more strained frameworks, leading to pronounced structural changes. In contrast, the sample with an L:M ratio of 0.5:1 showed higher uptake, plateauing around 6.3 wt % gravimetric and 30 g/L volumetric capacities. Although the two-step adsorption process was still present, it was less pronounced than in the lower L:M ratio sample, indicating increased framework stability with large pore volumes, as observed in higher ligand concentrations. The reduced hysteresis suggests that the energy barriers for the structural transitions were lower and the framework had better reversibility in the monoclinic phase. This monoclinic phase of this sample offers greater flexibility and pore expansion compared to those of the orthorhombic phase. The 1:1 ratio sample showed the highest H_2 uptake among the samples studied and exhibited no significant hysteresis. The lack of hysteresis suggested that the structural transitions were highly reversible, and the associated energy barriers were minimal, enabling the framework to revert to its initial state without significant holdup of the adsorbed gas volume within the crystal system. The isotherm displayed a similar initial uptake to the 0.52:1 sample but with a more pronounced step at the np to lp transition. The total gravimetric uptake reached 6.9 wt % at 70 bar, and the volumetric uptake was 38 g/L. This smooth isotherm indicated a more gradual and continuous adsorption process, reflective of a well-formed and stable framework structure. The high ligand concentration stabilizes the framework, reducing the distinctiveness of the two-step adsorption process and leading to a more continuous transition between the np and lp forms. This behavior was consistent with the monoclinic phase, which offers greater flexibility and larger pore volume compared with the orthorhombic phase. The L:M ratio significantly influenced the shape of the isotherm with no hysteresis and increased uptake capacity. The mechanism behind these transitions and hysteresis involved the flexibility of the MIL-53-Al framework, which can expand and contract in response to adsorption. At low pressures, the framework was primarily in a nanoparticle state, providing initial adsorption sites. However, as the pressure increased, the framework transitioned to an lp state, significantly increasing the pore volume and thereby storage capacity. This breathing effect was more pronounced in samples with higher ligand concentrations due to the enhanced structural flexibility provided by the additional ligands. Thus, optimizing the ligand concentration in MIL-53-Al is crucial for achieving the desired structural and adsorption properties, as evidenced by the highest uptake and smoothest isotherm in the 1:1 sample.

3.4. Determination of Working Capacity at 77 K between 70 and 5 Bar. The working or deliverable capacity of MOFs is determined as the difference in their total capacities between a completely filled tank pressure at 70 bar and an empty tank pressure at 5 bar.[25,55,56] The challenge of enhancing the working capacity of MOFs is thus 2-fold: to identify materials that drive the structural transitions above a certain pressure at practical temperatures and to ensure that these transitions are reversible with minimal energy barriers, allowing for efficient adsorption and desorption cycles. The computational studies in the literature revealed that achieving maximum H_2 working capacity at cryogenic temperatures (77 K) does not necessitate the presence of open metal sites with extremely strong interaction energies.[57] Due to the enhanced affinity provided by these sites, a significant proportion of adsorbed H_2 remains bound even at very low pressures. Consequently, a substantial amount of H_2 remains immobilized within the material, even when discharged at 5 bar, making it unavailable for fuel use. Conversely, near ambient temperatures (273 K), there is a preference for stronger and more accessible metal sites to maximize working capacity. This adjustment is crucial because isotherms exhibit flatter profiles at lower pressures, resulting in less H_2 remaining bound to the material after discharge. Materials with fewer open metal sites maintain consistent working capacities regardless of the binding strength at those sites, whereas those with more open metal sites exhibit higher working capacities as the binding strength decreases.[58]

The working capacity increased for all the MOFs employed under combined PS working conditions, as shown in Table 3. The 0.32:1 sample, with its orthorhombic structure, shows a gradual increase in H_2 uptake, resulting in lower volumetric (22 g/L) and gravimetric (4.7 wt %) uptake compared to the

https://doi.org/10.1021/acsanm.4c04072
ACS Appl. Nano Mater. 2024, 7, 23733−23743

Table 3. Determination of Gravimetric and Volumetric Working Capacities Based on the PS System Design

Sorbent (L:M)	Packing density (g/cm^3)	Gravimetric working capacity (wt %)	Volumetric working capacity (g/L)
0.32:1	0.28	4.7	22.5
0.52:1	0.35	5.8	29.07
1:1	0.38	6.7	37.22

monoclinic structures of the 0.5:1 and 1:1 samples. The 0.5:1 sample demonstrates intermediate performance with 29 g/L and 5.8 wt % uptakes, and the 1:1 sample displayed the highest total working capacities of 6.7 wt % and 37 g/L. These values clearly represent improvements in the gravimetric and volumetric storage capacity relative to isothermal PS conditions of the conventional MIL-53-Al.[59] In terms of working capacity, $(MIL\text{-}53\text{-}Al)_{1:1}$ stored about 15% higher than a compressed storage tank at 30.6 g/L (PS at 298 K). Hence, it is desirable to have a shallow increase in the low-pressure region that maximizes the working capacity of these MOFs. The $(MIL\text{-}53\text{-}Al)_{1:1}$ showed the highest working gravimetric uptake at 6.7 wt %, which was directly proportional to its BET surface area (Figure 9a). On a volumetric basis, the

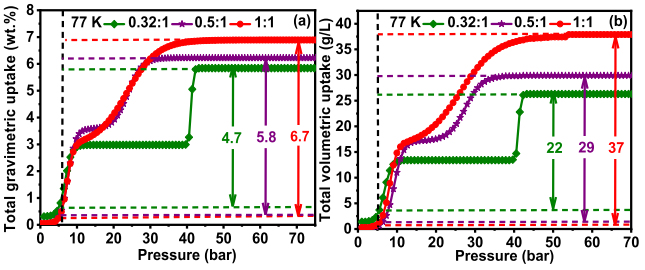

Figure 9. (a) Total gravimetric and (b) volumetric H_2 storage at 77 K and the working capacity between the full state for the combined PS capacity (77 K, 70 bar) and empty state (77 K, 5 bar) are indicated.

MOF possessed the highest capacity of 37 g/L (Figure 9b), originating from its reduced void fraction and high packing density (0.38 g/cm^3) within the system volume. The distinct isotherm shapes, characterized by a low uptake at low pressure and a high uptake at higher pressures, enhance the working capacity in PS systems by maximizing the difference between adsorption at low and high pressures. The crystal shape transitions, from orthorhombic to monoclinic, drive these changes, with monoclinic structures offering greater framework flexibility and larger pore volumes, allowing more adsorption. Additionally, the 1:1 sample's highest surface area (1906 m^2/g) and total pore volume (0.94 cm^3/g), along with its highest packing density (0.38 g/cm^3), contribute to its superior uptake. The improved packing density in monoclinic samples optimized the pore structure and accessibility, making them more efficient for H_2 storage. Thus, the monoclinic structure's steeper isotherms and higher packing densities enhanced their suitability for H_2 storage applications.

3.5. Determination of the Isosteric Heat of Adsorption. The isosteric heat of adsorption (Q_{st}) of H_2 over these MOFs correlated directly with the accessibility of metal nodes, as illustrated by the H_2 adsorption data presented in Figure 10. These findings highlight that metal nodes significantly enhance interactions with H_2 molecules at lower uptakes. Increasing the L:M ratio induced a transition from an orthorhombic to a

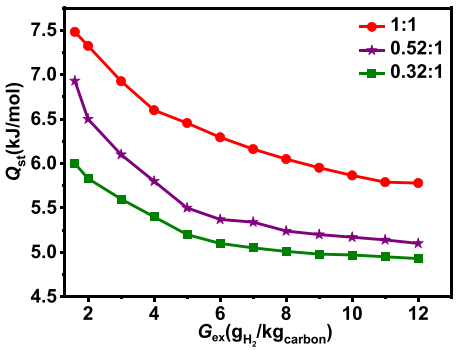

Figure 10. Isosteric heat of adsorption of H_2 over MIL-53-Al sorbents as a function of excess adsorption capacity.

monoclinic crystal orientation, further promoting stronger interactions with due to enhanced exposure of metal nodes. The isosteric heat of adsorption increased in the order of 6.0 kJ/mol < 6.8 kJ/mol < 7.5 kJ/mol for $(MIL\text{-}53\text{-}Al)_{0.32:1}$, $(MIL\text{-}53\text{-}Al)_{0.52:1}$, and $(MIL\text{-}53\text{-}Al)_{1:1}$, respectively. This trend reflected the rise in interaction energies, which can be attributed to the greater accessibility of metal nodes as the ligand-to-metal ratio increases.

As noted earlier, the enhanced H_2 adsorption was attributed to the monoclinic structure's flexibility, allowing greater framework expansion and creating more accessible adsorption sites. The XRD patterns revealed changes in the peak intensities corresponding to different crystallographic planes as the L:M ratio increased, supporting the phase transition and altered surface exposure. Specifically, the XPS peaks associated with Al, as seen in Figure 6d, showed increased intensities in the same order, highlighting that the change in the crystal shape has exposed the metal nodes, resulting in an increase in their adsorption energy. The higher BET surface areas and the larger pore volumes in the monoclinic phase provided more sites for H_2 adsorption, contributing to the increased isosteric heat of adsorption at higher uptakes. Additionally, the enhanced pore connectivity in the monoclinic phase facilitated easier diffusion of H_2 molecules, ensuring that adsorption sites are more readily accessible. The improved thermodynamic stability, indicated by higher isosteric heats, is crucial for practical H_2 storage applications, where efficient and reversible adsorption is necessary. Comparative studies of MOFs with varying L:M ratios and structural phases consistently showed higher isosteric heats for monoclinic structures, validating the role of crystal orientation and metal node exposure in enhancing H_2 interactions with the pore surface.

In addition to the adsorption capacity, the stability and regeneration of the MOFs under operational conditions are essential for their practical use. Monoclinic structures have demonstrated better structural stability and reversibility under multiple adsorption−desorption cycles, making them more suitable for repeated use in H_2 storage applications. The ability to maintain high performance over numerous cycles underscored the robustness of the monoclinic phase. Moreover, tuning the crystal orientation through optimizing the L:M ratio offered a facile pathway to design efficient MOFs for specific H_2 storage requirements. By precise control of the synthesis parameters, it is possible to tailor the structural properties to achieve the desired adsorption characteristics. This tunability highlights the versatility of MOFs and their potential for customized applications in energy storage

https://doi.org/10.1021/acsanm.4c04072
ACS Appl. Nano Mater. 2024, 7, 23733−23743

technologies. By considering these additional points, we thoroughly validate the relationship between the isosteric heat of adsorption, crystal orientation, and metal node exposure in MOFs, highlighting the critical factors that contribute to improved H_2 storage performance and practical application feasibility.

Figure 11 illustrates the comparison of the working capacity of the systems when employed under charge−discharge PS

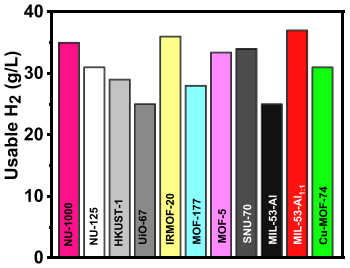

Figure 11. Comparison of H_2 working capacity of benchmark sorbents based on the charge−discharge cycle.

conditions such as (77 K, 100−5 bar pressure), respectively. The working capacities of several benchmark sorbents, such as NU-1000, NU-125, UiO-67, MOF-177, MOF-5, HKUST-1, IRMOF-20, SNU-70, MIL-53-Al, and Cu-MOF-74, were also compared with this work, as obtained from the literature.[28,60] While $(MIL\text{-}53\text{-}Al)_{1:1}$ in this study achieved an H_2 working capacity of around 37 g/L, which is slightly lower than some of the benchmark materials such as IRMOF-20 and NU-1000, it represents a notable 32% improvement over the parent MIL-53-Al.[59] Despite its moderate surface area (1906 m^2/g), its enhanced volumetric capacity primarily stemmed from its increased packing density (0.38 g/cm^3), allowing it to compare favorably to the benchmark sorbents like MOF-5. This enhancement underscores the significance of the breathing transition and densification strategies in optimizing the storage performance of MOFs, where structural flexibility has been found to promote the working capacities. The breathing mechanism, which also allows for improved packing density without compromising structural integrity, has demonstrated potential as an effective strategy for enhancing H_2 storage capacities. This approach could be applied to other MOFs, potentially unlocking further storage capacity improvements. Moreover, the functionalization of these frameworks with additional open metal sites or the incorporation of bimetallic nodes could significantly improved H_2 interactions in $(MIL\text{-}53\text{-}Al)_{1:1}$. Such modifications may enable future iterations of these materials to rival or surpass the performance of the leading sorbents.

4. CONCLUSIONS

This study elucidated the critical impact of crystal morphology engineering on the H_2 storage performance of MIL-53-Al sorbent. Through systematic manipulation of the L:M ratio during synthesis, we successfully tailored the crystal size and shape distributions of MIL-53-Al, resulting in significant advancements in packing density and volumetric H_2 storage capacity. Specifically, the engineered MOF samples with a bimodal distribution of monoclinic and orthorhombic crystal shapes achieved a notable packing density of 0.38 g/cm^3. This enhancement not only optimized pore space utilization but also led to a substantial 32% increase in volumetric working capacity compared to unmodified MIL-53-Al, marking a significant stride toward overcoming the limitations of traditional H_2 storage methods. Furthermore, our investigation into high-pressure H_2 adsorption isotherms highlighted the correlation between crystal morphology and adsorption behavior. Samples with higher L ratios, $(MIL\text{-}53\text{-}Al)_{1:1}$, exhibited enhanced gravimetric and volumetric working capacities, reaching up to 6.7 wt % and 37 g/L, respectively, under PS conditions at 77 K between 70 and 5 bar. This improvement was facilitated by the engineered crystal shapes, which promoted efficient adsorption−desorption cycles and minimized high-pressure conditions to achieve optimal H_2 saturation capacities. The observed isotherm shapes, characterized by distinct transitions from narrow-pore to large-pore structures, underscore the efficacy of crystal morphology engineering in optimizing the H_2 storage performance at practical temperatures and pressures.

Moreover, the ability to tailor MOF structures for enhanced performance not only addresses current challenges in H_2 storage but also positions MOFs as versatile materials for future energy storage applications under various environmental conditions. Continued research efforts in optimizing crystal morphology and exploring novel synthesis strategies will be pivotal in harnessing the full potential of MOFs to meet growing energy demands sustainably. In conclusion, this study provides compelling evidence that crystal morphology engineering significantly enhances the H_2 storage properties of MOFs, paving a facile pathway for their widespread adoption in the renewable energy sectors. Our findings highlight the pivotal role of fundamental material design principles in advancing sustainable and efficient energy storage solutions, setting a foundation for continued innovation in MOF-based technologies.

■ ASSOCIATED CONTENT

Supporting Information

The Supporting Information is available free of charge at https://pubs.acs.org/doi/10.1021/acsanm.4c04072.

Micropore size distribution; thermogravimetric analysis (TGA) and XRD characterization; particle size distribution; packing density estimation; high-pressure hydrogen adsorption measurements; XPS elemental composition (PDF)

■ AUTHOR INFORMATION

Corresponding Author

Fateme Rezaei − *Department of Chemical, Environmental and Materials Engineering, University of Miami, Coral Gables, Florida 33124, United States;* orcid.org/0000-0002-4214-4235; Email: rezaeif@miami.edu

Authors

Ruthradharshini Murugavel − *Department of Chemical, Environmental and Materials Engineering, University of Miami, Coral Gables, Florida 33124, United States*

Ali A. Rownaghi − *United States Department of Energy, National Energy Technology Laboratory (NETL), Pittsburgh, Pennsylvania 15236-0940, United States;* orcid.org/0000-0001-5228-5624

Complete contact information is available at: https://pubs.acs.org/10.1021/acsanm.4c04072

https://doi.org/10.1021/acsanm.4c04072
ACS Appl. Nano Mater. 2024, 7, 23733−23743

Notes

The authors declare no competing financial interest.

■ ACKNOWLEDGMENTS

We thank the National Science Foundation for financially supporting this project through the NSF-PFI-2044726 grant.

■ REFERENCES

(1) Al-Naddaf, Q.; Majedi Far, H.; Cheshomi, N.; Rownaghi, A. A.; Rezaei, F. Exceptionally High Gravimetric Methane Storage in Aerogel-Derived Carbons. *Ind. Eng. Chem. Res.* **2020**, *59* (43), 19383−19391.

(2) Al-Naddaf, Q.; Al-Mansour, M.; Thakkar, H.; Rezaei, F. MOF-GO Hybrid Nanocomposite Adsorbents for Methane Storage. *Ind. Eng. Chem. Res.* **2018**, *57* (51), 17470−17479.

(3) Bosu, S.; Rajamohan, N. Recent Advancements in Hydrogen Storage - Comparative Review on Methods, Operating Conditions and Challenges. *Int. J. Hydrogen Energy* **2024**, *52*, 352−370.

(4) Muhammed, N. S.; Haq, B.; Al Shehri, D.; Al-Ahmed, A.; Rahman, M. M.; Zaman, E. A Review on Underground Hydrogen Storage: Insight into Geological Sites, Influencing Factors and Future Outlook. *Energy Rep.* **2022**, *8*, 461−499.

(5) Petitpas, G.; Bénard, P.; Klebanoff, L. E.; Xiao, J.; Aceves, S. A Comparative Analysis of the Cryo-Compression and Cryo-Adsorption Hydrogen Storage Methods. *Int. J. Hydrogen Energy* **2014**, *39* (20), 10564−10584.

(6) Lee, S.-Y.; Lee, J.-H.; Kim, Y.-H.; Kim, J.-W.; Lee, K.-J.; Park, S.-J. Recent Progress Using Solid-State Materials for Hydrogen Storage: A Short Review. *Processes* **2022**, *10* (2), 304.

(7) Murugavel, R.; Rownaghi, A. A.; Rezaei, F. Effect of Alkali Metal Functionalization on Hydrogen Storage Performance of Highly Porous Activated Carbons. *Energy & Fuels* **2023**, *37* (23), 19292−19303.

(8) Blankenship, L. S.; Balahmar, N.; Mokaya, R. Oxygen-Rich Microporous Carbons with Exceptional Hydrogen Storage Capacity. *Nat. Commun.* **2017**, *8*, 1545.

(9) Schaefer, S.; Fierro, V.; Izquierdo, M. T.; Celzard, A. Assessment of Hydrogen Storage in Activated Carbons Produced from Hydrothermally Treated Organic Materials. *Int. J. Hydrogen Energy* **2016**, *41* (28), 12146−12156.

(10) Kostoglou, N.; Koczwara, C.; Stock, S.; Tampaxis, C.; Charalambopoulou, G.; Steriotis, T.; Paris, O.; Rebholz, C.; Mitterer, C. Nanoporous Polymer-Derived Activated Carbon for Hydrogen Adsorption and Electrochemical Energy Storage. *Chem. Eng. J.* **2022**, *427*, 131730.

(11) Kumar, S.; Vijayan, S.; Goyal, K.; Kathuria, M.; Gulati, S. Functionalization Strategies of Metal−Organic Frameworks (MOFs): Diverse Ways to Versatile MOFs. In *Metal-Organic Frameworks (MOFs) as Catalysts*, Gulati, S., Ed.; Springer Nature Singapore: Singapore, 2022; pp. 99123.

(12) Sule, R.; Mishra, A. K.; Nkambule, T. T. Recent Advancement in Consolidation of MOFs as Absorbents for Hydrogen Storage. *Int. J. Energy Res.* **2021**, *45* (9), 12481−12499.

(13) Almáši, M. Chapter 28 - Current Development in MOFs for Hydrogen Storage: A Mechanistic Investigation. In *Metal-Organic Framework-Based Nanomaterials for Energy Conversion and Storage*; Gupta, R. K.; Nguyen, T. A.; Yasin, G., Eds.; Elsevier, 2022; pp. 631661.

(14) Furukawa, H.; Yaghi, O. M. Storage of Hydrogen, Methane, and Carbon Dioxide in Highly Porous Covalent Organic Frameworks for Clean Energy Applications. *J. Am. Chem. Soc.* **2009**, *131* (25), 8875−8883.

(15) Cao, D.; Lan, J.; Wang, W.; Smit, B. Lithium-Doped 3D Covalent Organic Frameworks: High-Capacity Hydrogen Storage Materials. *Angew. Chem., Int. Ed.* **2009**, *48* (26), 4730−4733.

(16) Han, S. S.; Furukawa, H.; Yaghi, O. M.; Goddard, W. A. I. I. I. Covalent Organic Frameworks as Exceptional Hydrogen Storage Materials. *J. Am. Chem. Soc.* **2008**, *130* (35), 11580−11581.

(17) Tang, Z.; Chen, J.; Xu, Y.; Li, Z.; Sheng, L.; Hu, Y.; Wang, X.; Wang, J.; Tang, Y.; He, X.; Xu, H. Lithium-Induced Covalent Organic Frameworks with Enhanced Sorption Heat for Efficient Hydrogen Storage. *Chem. Mater.* **2024**, *36* (9), 4437−4443.

(18) Cousins, K.; Zhang, R. Highly Porous Organic Polymers for Hydrogen Fuel Storage. *Polymers* **2019**, *11* (4), 690.

(19) Sun, Y.; Ben, T.; Wang, L.; Qiu, S.; Sun, H. Computational Design of Porous Organic Frameworks for High-Capacity Hydrogen Storage by Incorporating Lithium Tetrazolide Moieties. *J. Phys. Chem. Lett.* **2010**, *1* (19), 2753−2756.

(20) Xia, Y.; Cao, H.; Xu, F.; Chen, Y.; Xia, Y.; Zhang, D.; Dai, L.; Qu, K.; Lian, C.; Huang, K.; Xing, W.; Jin, W.; Xu, Z. Polymeric Membranes with Aligned Zeolite Nanosheets for Sustainable Energy Storage. *Nat. Sustainable* **2022**, *5* (12), 1080−1091.

(21) Wang, S.; Hu, R.; Ren, J.; Lv, Y.; Song, L.; Zhao, H.; Jiang, X.; Gao, D.; Chen, G. Surface Hydrophobization of Zeolite Enables Mass Transfer Matching in Gas-Liquid-Solid Three-Phase Hydrogenation under Ambient Pressure. *Nat. Commun.* **2024**, *15* (1), 2076.

(22) Dong, J.; Wang, X.; Xu, H.; Zhao, Q.; Li, J. Hydrogen Storage in Several Microporous Zeolites. *Int. J. Hydrogen Energy* **2007**, *32* (18), 4998−5004.

(23) Murugavel, R.; Rownaghi, A.A.; Rezaei, F. Engineering Microstructure of Ultraporous Carbon Aerogels as Advanced H_2 Sorbent Carriers. *Chem. Mater.* **2024**, *36* (18), 8565−8577.

(24) Hu, Y. H.; Zhang, L. Hydrogen Storage in Metal−Organic Frameworks. *Adv. Mater.* **2010**, *22* (20), No. E117−E130.

(25) Ahmed, A.; Liu, Y.; Purewal, J.; Tran, L. D.; Wong-Foy, A. G.; Veenstra, M.; Matzger, A. J.; Siegel, D. J. Balancing Gravimetric and Volumetric Hydrogen Density in MOFs. *Energy Environ. Sci.* **2017**, *10* (11), 2459−2471.

(26) Peng, P.; Jiang, H. Z. H.; Collins, S.; Furukawa, H.; Long, J. R.; Breunig, H. Long Duration Energy Storage Using Hydrogen in Metal−Organic Frameworks: Opportunities and Challenges. *ACS Energy Lett.* **2024**, *9* (6), 2727−2735.

(27) Pham, T. D.; Sengupta, D.; Farha, O. K.; Snurr, R. Q. Investigation of Anionic Metal−Organic Frameworks with Extra-Framework Cations for Room Temperature Hydrogen Storage. *Chem. Mater.* **2024**, *36* (8), 3794−3802.

(28) Zhang, R.; Daglar, H.; Tang, C.; Li, P.; Feng, L.; Han, H.; Wu, G.; Limketkai, B. N.; Wu, Y.; Yang, S.; Chen, A. X.-Y.; Stern, C. L.; Malliakas, C. D.; Snurr, R. Q.; Stoddart, J. F. Balancing Volumetric and Gravimetric Capacity for Hydrogen in Supramolecular Crystals. *Nat. Chem.* **2024**, 1−7.

(29) Bai, X.-J.; Yang, C.; Tang, Z. Enabling Long-Distance Hydrogen Spillover in Nonreducible Metal-Organic Frameworks for Catalytic Reaction. *Nat. Commun.* **2024**, *15* (1), 6263.

(30) Gu, Z.; Li, M.; Chen, C.; Zhang, X.; Luo, C.; Yin, Y.; Su, R.; Zhang, S.; Shen, Y.; Fu, Y.; Zhang, W.; Huo, F. Water-assisted hydrogen spillover in Pt nanoparticle-based metal−organic framework composites. *Nat. Commun.* **2023**, *14* (1), 5836.

(31) Shun, K.; Mori, K.; Kidawara, T.; Ichikawa, S.; Yamashita, H. Heteroatom Doping Enables Hydrogen Spillover via H+/E− Diffusion Pathways on a Non-Reducible Metal Oxide. *Nat. Commun.* **2024**, *15* (1), 6403.

(32) Park, Y.-J.; Lee, H.; Choi, H. L.; Tapia, M. C.; Chuah, C. Y.; Bae, T.-H. Mixed-Dimensional Nanocomposites Based on 2D Materials for Hydrogen Storage and CO_2 Capture. *Npj 2D Mater. Appl.* **2023**, *7* (1), 61.

(33) Purewal, J. J.; Liu, D.; Yang, J.; Sudik, A.; Siegel, D. J.; Maurer, S.; Müller, U. Increased Volumetric Hydrogen Uptake of MOF-5 by Powder Densification. *Int. J. Hydrogen Energy* **2012**, *37* (3), 2723−2727.

(34) Zacharia, R.; Cossement, D.; Lafi, L.; Chahine, R. Volumetric Hydrogen Sorption Capacity of Monoliths Prepared by Mechanical Densification of MOF-177. *J. Mater. Chem.* **2010**, *20* (11), 2145−2151.

(35) Madden, D. G.; O'Nolan, D.; Rampal, N.; Babu, R.; Çamur, C.; Al Shakhs, A. N.; Zhang, S.-Y.; Rance, G. A.; Perez, J.; Casati, N. P. M.; et al. Densified HKUST-1 Monoliths as a Route to High

https://doi.org/10.1021/acsanm.4c04072
ACS Appl. Nano Mater. 2024, 7, 23733−23743

Volumetric and Gravimetric Hydrogen Storage Capacity. *J. Am. Chem. Soc.* **2022**, *144* (30), 13729−13739.
(36) Lawson, S.; Li, X.; Thakkar, H.; Rownaghi, A. A.; Rezaei, F. Recent Advances in 3D Printing of Structured Materials for Adsorption and Catalysis Applications. *Chem. Rev.* **2021**, *121* (10), 6246−6291.
(37) *Hydrogen Strategy, Enabling a Low Carbon Economy; Office of Fossil Energy*; U.S. Department of Energy: Washington, DC, 2020.
(38) *The Future of Hydrogen*; Seizing Today's Opportunities, 2019.
(39) *Foundational Science for Carbon-Neutral Hydrogen Technologies Technology Status Document Basic Energy Sciences Virtual Roundtable Co-Chairs Acknowledgement to DOE*. Energy Efficiency & Renewable Energy, Hydrogen and Fuel Cell Technologies Office Eric Miller. DOE-EERE-HFTO. 2021.
(40) Siegel, D. J.; Hardy, B. *Engineering an Adsorbent-Based Hydrogen Storage System: What Have We Learned?*; HSECoE: Golden, CO, 2015.
(41) Suresh, K.; Aulakh, D.; Purewal, J.; Siegel, D. J.; Veenstra, M.; Matzger, A. J. Optimizing Hydrogen Storage in MOFs through Engineering of Crystal Morphology and Control of Crystal Size. *J. Am. Chem. Soc.* **2021**, *143* (28), 10727−10734.
(42) Samantaray, S. S.; Putnam, S. T.; Stadie, N. P. Volumetrics of Hydrogen Storage by Physical Adsorption. *Inorganics* **2021**, *9* (6), 45.
(43) Connolly, B. M.; Madden, D. G.; Wheatley, A. E. H.; Fairen-Jimenez, D. Shaping the Future of Fuel: Monolithic Metal−Organic Frameworks for High-Density Gas Storage. *J. Am. Chem. Soc.* **2020**, *142* (19), 8541−8549.
(44) Blanita, G.; Coldea, I.; Misan, I.; Lupu, D. Hydrogen Cryo-Adsorption by Hexagonal Prism Monoliths of MIL-101. *Int. J. Hydrogen Energy* **2014**, *39* (30), 17040−17046.
(45) Ahadi, N.; Askari, S.; Fouladitajar, A.; Akbari, I. Facile Synthesis of Hierarchically Structured MIL-53(Al) with Superior Properties Using an Environmentally-Friendly Ultrasonic Method for Separating Lead Ions from Aqueous Solutions. *Sci. Rep.* **2022**, *12* (1), 2649.
(46) Rowsell, J. L. C.; Yaghi, O. M. Metal−Organic Frameworks: A New Class of Porous Materials. *Microporous Mesoporous Mater.* **2004**, *73* (1), 3−14.
(47) Loiseau, T.; Serre, C.; Huguenard, C.; Fink, G.; Taulelle, F.; Henry, M.; Bataille, T.; Férey, G. A Rationale for the Large Breathing of the Porous Aluminum Terephthalate (MIL-53) Upon Hydration. *Chem.−Eur. J.* **2004**, *10* (6), 1373−1382.
(48) Kim, S.-Y.; Kang, J. H.; Kim, S.-I.; Bae, Y.-S. Extraordinarily Large and Stable Methane Delivery of MIL-53(Al) under LNG-ANG Conditions. *Chem. Eng. J.* **2019**, *365*, 242−248.
(49) Taheri, A.; Babakhani, E. G.; Towfighi, J. Study of Synthesis Parameters of MIL-53(Al) Using Experimental Design Methodology for CO_2/CH_4 Separation. *Adsorpt. Sci. Technol.* **2018**, *36*, 247−269.
(50) Nanthamathee, C.; Ling, S.; Slater, B.; Attfield, M. P. Contradistinct Thermoresponsive Behavior of Isostructural MIL-53 Type Metal−Organic Frameworks by Modifying the Framework Inorganic Anion. *Chem. Mater.* **2015**, *27* (1), 85−95.
(51) Ge, J.; Liu, L.; Qiu, L.; Jiang, X.; Shen, Y. Facile Synthesis of Amine-Functionalized MIL-53(Al) by Ultrasound Microwave Method and Application for CO_2 Capture. *J. Porous Mater.* **2016**, *23* (4), 857−865.
(52) Kim, J. Y.; Zhang, L.; Balderas-Xicohténcatl, R.; Park, J.; Hirscher, M.; Moon, H. R.; Oh, H. Selective Hydrogen Isotope Separation via Breathing Transition in MIL-53(Al). *J. Am. Chem. Soc.* **2017**, *139* (49), 17743−17746.
(53) Pollock, R. A.; Her, J.-H.; Brown, C. M.; Liu, Y.; Dailly, A. Kinetic Trapping of D_2 in MIL-53(Al) Observed Using Neutron Scattering. *J. Phys. Chem. C* **2014**, *118* (31), 18197−18206.
(54) Ashling, C. W.; Johnstone, D. N.; Widmer, R. N.; Hou, J.; Collins, S. M.; Sapnik, A. F.; Bumstead, A. M.; Midgley, P. A.; Chater, P. A.; Keen, D. A.; Bennett, T. D. Synthesis and Properties of a Compositional Series of MIL-53(Al) Metal−Organic Framework Crystal-Glass Composites. *J. Am. Chem. Soc.* **2019**, *141* (39), 15641−15648.
(55) García-Holley, P.; Schweitzer, B.; Islamoglu, T.; Liu, Y.; Lin, L.; Rodriguez, S.; Weston, M. H.; Hupp, J. T.; Gómez-Gualdrón, D. A.; Yildirim, T.; Farha, O. K. Benchmark Study of Hydrogen Storage in Metal−Organic Frameworks under Temperature and Pressure Swing Conditions. *ACS Energy Lett.* **2018**, *3* (3), 748−754.
(56) Schlichtenmayer, M.; Hirscher, M. The Usable Capacity of Porous Materials for Hydrogen Storage. *Appl. Phys. A: Mater. Sci. Process.* **2016**, *122* (4), 379.
(57) Goldsmith, J.; Wong-Foy, A. G.; Cafarella, M. J.; Siegel, D. J. Theoretical Limits of Hydrogen Storage in Metal−Organic Frameworks: Opportunities and Trade-Offs. *Chem. Mater.* **2013**, *25*, 3373−3382.
(58) Allendorf, M. D.; Hulvey, Z.; Gennett, T.; Ahmed, A.; Autrey, T.; Camp, J.; Seon Cho, E.; Furukawa, H.; Haranczyk, M.; Head-Gordon, M.; Jeong, S.; Karkamkar, A.; Liu, D.-J.; Long, J. R.; Meihaus, K. R.; Nayyar, I. H.; Nazarov, R.; Siegel, D. J.; Stavila, V.; Urban, J. J.; Veccham, S. P.; Wood, B. C. An Assessment of Strategies for the Development of Solid-State Adsorbents for Vehicular Hydrogen Storage. *Energy Environ. Sci.* **2018**, *11* (10), 2784−2812.
(59) Férey, G.; Latroche, M.; Serre, C.; Millange, F.; Loiseau, T.; Percheron-Guégan, A. Hydrogen Adsorption in the Nanoporous Metal-Benzenedicarboxylate $M(OH)(O_2C-C_6H_4-CO_2)$ ($M = Al^{3+}$, Cr^{3+}), MIL-53. *Chem. Commun.* **2003**, No. 24, 2976−2977.
(60) Ahmed, A.; Seth, S.; Purewal, J.; Wong-Foy, A. G.; Veenstra, M.; Matzger, A. J.; Siegel, D. J. Exceptional Hydrogen Storage Achieved by Screening Nearly Half a Million Metal-Organic Frameworks. *Nat. Commun.* **2019**, *10* (1), 1568.

https://doi.org/10.1021/acsanm.4c04072
ACS Appl. Nano Mater. 2024, 7, 23733−23743